QCL-Based Cryogen-Free THz Optical Wireless Communication Link

Alessia Sorgi, Marco Meucci, Muhammad A. Umair, Francesco Cappelli, Guido Toci, Paolo De Natale, Leonardo Viti, Andrea C. Ferrari, Miriam S. Vitiello, Luigi Consolino, and Jacopo Catani**

The increased demand for high-speed (terabit-per-second) wireless data transmission has driven the shift of the frequency carrier from ubiquitous radio frequency systems toward the 1–5 THz range, triggering a new interest for THz quantum cascade laser (QCL)-based free-space optical (FSO) links. As compared to standard telecom-band FSO links, platforms based on THz frequency sources are inherently robust against Rayleigh scattering. Atmospheric absorption, mainly due to water vapor, limits the achievable link distance range, but at the same time, it shifts channel security on the physical layer. THz QCL-based FSO links are reported with setups requiring cryogenic cooling, seriously limiting their development for mass applications. Here, a cryogen-free, transportable THz FSO communication system is presented relying on a directly modulated 2.83 THz QCL transmitter, hosted in a closed-cycle Stirling cryocooler, and exploiting a room-temperature graphene-based receiver, implementing a binary on-off keying modulation scheme with Manchester encoding. Power-versus-distance measurements and communication tests are performed, and propose a propagation model to extrapolate the performances of the THz link in an optimized configuration. This approach reduces complexity and costs, as compared to the state-of-the-art THz FSO links, and paves the way for the deployment of optical wireless communication systems exploiting the 1–5 THz frequency range.

1. Introduction

Wireless data traffic has been steadily growing in the last two decades,[1] and this trend is expected to continue, with a foreseen increase in global mobile data traffic of a factor ≈4 from 2022 (90 Exabyte per month) to 2028 (>300 Exabyte per month).[2] The growth of the internet of things (IoT) and the emergence of new services (e.g., augmented reality,[3] telemedicine,[4–5] brain-computer interfaces,[6–7] and autonomous systems[8]) require ultra-high capacity (≈1 terabit per second -Tbps[9]) connectivity and high-density access networks with high-reliability (99.999%) and low (≈1 ms) end-to-end delays.[10–15] The 5th generation communication network (5G) will not meet the target requirements before late ‘20s, and the target Gbps rates may fall short in supporting the aforementioned applications that require several hundred Gbps to several Tbps data rates with low latency (< 1 ms).[16] The future 6G vision aims at overcoming the limitations connected

A. Sorgi, M. Meucci, M. A. Umair, F. Cappelli, G. Toci, P. De Natale, L. Consolino, J. Catani
CNR-Istituto Nazionale di Ottica
(CNR-INO)
Via N. Carrara 1, Sesto Fiorentino (FI), FI 50019, Italy
E-mail: luigi.consolino@ino.cnr.it; jacopo.catani@ino.cnr.it

A. Sorgi, M. Meucci, M. A. Umair, F. Cappelli, P. De Natale, L. Consolino, J. Catani
European Laboratory for Non-Linear Spectroscopy
LENS
Via N. Carrara 1, Sesto Fiorentino, FI 50019, Italy

L. Viti, M. S. Vitiello
NEST, CNR-Istituto Nanoscienze and Scuola Normale Superiore
Piazza San Silvestro 12, Pisa 56127, Italy

A. C. Ferrari
Cambridge Graphene Centre, University of Cambridge
Cambridge CB3 0FA, UK

The ORCID identification number(s) for the author(s) of this article can be found under https://doi.org/10.1002/lpor.202301082

DOI: 10.1002/lpor.202301082

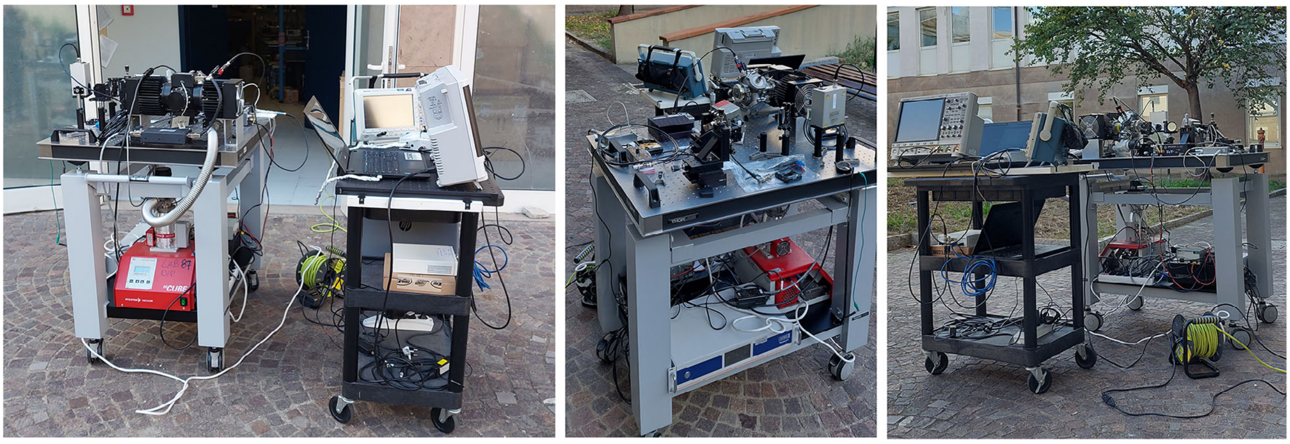

Figure 1. Picture of setup: the black cart carries the digital TX and RX sub-blocks, while the gray cart mounts the breadboard with an FSO link between the QCL, hosted in the closed-cycle cryocooler, the room-temperature GFET detector, and carries both the source and receiver supporting electronics and the turbomolecular vacuum pump.

to the increasing radio-frequency (RF) spectrum crunch,[17] exploiting a much broader frequency range, by encompassing the full optical spectrum for the deployment of cooperative, pervasive wireless data exchange platforms based on optical wireless communication (OWC).[18] One of the key advantages of THz wireless communication (TWC) over conventional RF or mm-wave broadcasting is the higher carrier frequency, allowing larger bit rates and data transmission speed.[19] Furthermore, with respect to visible or near-IR free space optical communication (FSOC) a terrestrial TWC channel is inherently robust against Rayleigh scattering (scaling with the radiation wavelength as λ^{-4}) by dust, smoke, and particulates dispersed in the atmosphere, with potential advantages in harsh and industrial environments.

However, while THz radiation is much less exposed to Rayleigh scattering, it is prone to atmospheric absorption,[20] mostly due to water vapor,[20] currently limiting the link distance range in the air to a few meters.[27] TWC is still of interest for applications such as fast and secure short-range terrestrial communications or inter-satellite links (ISLs), where path loss due to molecular absorption is not an issue and is, on the contrary, a great advantage in terms of security, as orbital THz communications cannot be intercepted from the ground.[21] THz radiation provides additional advantages for ISLs, such as more relaxed pointing constraints with respect to visible and near-infrared communication,[22] reduction of power consumption due to solid-state transmitter (TX) and receiver (RX) devices, and satellite payload, thanks to plastic-made optical elements.

Despite the interest in TWC systems, presently, only the 0.3–0.6 THz region has been explored for wireless communication links based on sub-THz electronic devices[19,23,24] assisted by photonic technology.[25–27] The development of TWC systems >1 THz has been hindered by the unavailability of efficient sources and photodetectors (PDs). So far, TWC setups have been based on QCLs sources[28] and quantum well-infrared photodetectors (QWIPs)[29] as active elements, both requiring deep cryogenic cooling ($T \approx 10$ K), with reported data rates up to 20 Mbps over distances of ≈2 m.[30–32] The complexity of these implementations has hindered the deployment of THz technologies both for terrestrial and satellite realistic applications.

Recently, QCLs with high operating temperatures (up to 250 K) have been reported,[33] as well as fast and sensitive PDs (with noise equivalent power NEP < 100 pWHz$^{-1/2}$ and response times < 1 ns) operating at room temperature (RT). These are based on either standard commercial technologies, such as Schottky diodes[34,35] and Si-based MOSFETs,[36] or innovative materials, such as graphene.[37,38] Moreover, it is known that mid-IR QCLs can be modulated at frequencies in the tens of GHz range[39] and that a theoretical limit to the modulation frequency of THz QCLs is set to hundreds of GHz by the ps carrier lifetime.[40] However, the realization of transportable setups, with no need for complex laboratory facilities remains a challenge.

Here, we report a transportable THz FSOC link based on a 2.83 THz QCL transmitter, and an RT, solid-state, graphene field-effect transistor (GFET) as a receiver. This operates with no need for liquid He cooling for either TX or RX stages. The whole setup, including supporting electronics and turbomolecular vacuum pump, fits on a movable cart (**Figure 1**). We characterize the THz channel in terms of achievable signal-to-noise ratio (SNR), as well as of THz communication performances as a function of the effective distance between TX and RX stages, using custom digital signal processing (DSP) filtering for excess noise suppression. This low-power-consumption, small-footprint, and cryogen-free setup pave the way to transportable, terrestrial field-deployable, and satellite-compatible THz links operating in the 1–5 THz range.

2. Experimental Setup

This section describes the system architecture (Section 2.1) and the hardware components (Section 2.2) employed to realize the TWC link, whilst experimental procedures are described in Section 3.

2.1. THz OWC System Model

Figure 2 shows that our TWC system can be split into a transmitter block, TX, an optical free-space channel, and a receiver

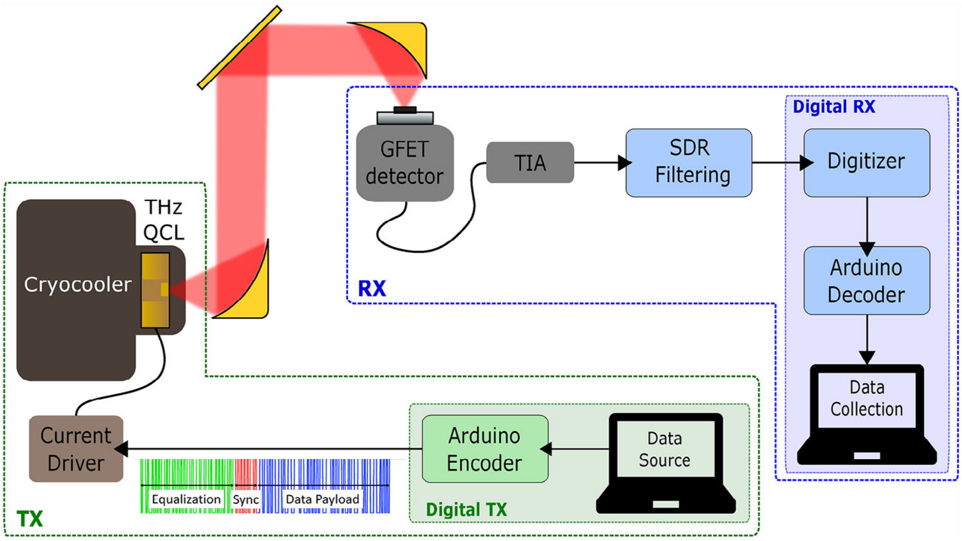

Figure 2. Schematic of set-up: The lower panel shows the TX block diagram, with a sub-block for digital encoding, based on an Arduino DUE board. TX generates a stream of packets, sent through the FSO link that includes a QCL hosted in a Stirling cryocooler, and a RT GFET PD. The upper panel shows the RX block diagram with a sub-block for digital decoding, performed through a second Arduino DUE board. The output of the GFET PD passes through a variable-gain TIA, then the signal is filtered through an SDR-based DSP filtering stage. Subsequently, the digitization of the signal takes place through a single-threshold Schmitt comparator, decoded through a second Arduino DUE board, also performing a byte-wise comparison for PER calculation.

block, RX. Both TX and RX can be further divided into digital TX and RX sub-blocks for encoding and decoding of data streams, and in analog, electro-optical front-ends for the generation and detection of THz radiation. The TX digital board can generate a stream of digital packets at different bit rates. The digital information is encoded in the THz QCL source as intensity modulation between 0% (laser below threshold) and 100% (laser turned on at nominal power ≈1 mW) through On-Off Keying (OOK) modulation scheme with Manchester encoding.[41] The modulated THz beam reaches the RX stage and is converted into an electric signal by a GFET PD. A variable-gain transimpedance amplifier (TIA) boosts the signal, and a digital filter, implemented through a software-defined radio (SDR)-based DSP stage removes excess noise before passing it to a digitizer/decoder stage, realized through a second RX digital board. This unit counts the correctly received packets comparing each with a reference message pre-stored on the board, and the Packet Error Rate (PER) is calculated as the ratio of the number of correctly received packets (as decoded by the RX unit) to the total number of packets sent by the TX on each experimental run, corresponding to 10^5. This sets an error-free threshold to PER$<10^{-5}$. In our architecture, the packet framing consists of 2 pre-equalization bytes (to minimize the effects of intensity transients at the onset of each packet), a 1-byte synchronization pattern, used to recover the TX-RX synchronization, and a 4-byte data payload.

2.2. Hardware Description–TX Stage

The TX digital sub-block is based on digital open-source microcontroller boards (Arduino DUE[42]). This is motivated by the considerable processing capacity (84 MHz clock), small card-size form factor, with reduced costs and dimensions of Arduino DUE platform.[42] These boards were previously implemented in OWC and Visible Light Communications (VLC) links in different applications up to 5 Mbps.[43,44] The digital message is encoded as intensity modulation into the THz beam by injecting the digital signal into the analog current modulation input of the driver (QCL2000, Wavelength Electronics) of the THz source. The analog modulation input allows for digital modulations with ≈250 ns fall and rise times, corresponding to a bandwidth (BW) ≈1.4 MHz. The optical laser source is a QCL emitting at 2.83 THz, based on a bound-to-continuum active region, included in a 150 µm wide single-plasmon ridge waveguide, cleaved to form a 2 mm Fabry–Perot cavity, allowing an optical peak-power of 100 mW at 4 K in pulsed operation.[45] This type of active region has shown high wall-plug efficiencies (WPE) when driven in continuous-wave (CW),[45] giving access to operational temperatures attainable by compact closed-cycle cryostats, thus eliminating the need for cumbersome liquid-He tanks. The QCL device employed in our setup features a lower WPE (≈0,11% @38.4 K) as compared to liquid-He-based implementations,[45] probably due to a lower cooling power of the closed-cycle cryostat, and/or by a non-optimal device thermal contact. This limits the maximum power emitted by the device but does not affect the characterization of our TWC link in any way. Our device is hosted in a small-footprint (50 × 15 × 15 cm^3) Stirling cryocooler (Ricor, model K353), suitable for transportable solutions, reaching a base temperature ≈26 K, and stabilizing at 38.4 K when the QCL is driven with a continuous current of 570 mA. This experimental condition is chosen for the maximum device output power ≈1 mW. The radiation emitted by the QCL is collimated by a 90° off-axis parabolic mirror with 1″ effective focal length (EFL) and 1″ clear aperture, and it is then focused by an identical parabolic mirror onto the PD. The optical path between QCL and PD is 60 cm long.

2.3. Hardware Description - RX Stage

The PD is an antenna-coupled, GFET.[46] The active element is a conductive channel constituted by a high-mobility (μ = 38 000 cm^2 V^{-1} s^{-1}) exfoliated flake of single-layer graphene (SLG), encapsulated in hexagonal boron nitride (hBN) flakes[46] (more details on device fabrication and geometry are provided in the Supporting Information). The 20 μm radius bow-tie antenna is asymmetrically connected to the source (s) and gate (g) electrodes of the GFET, defining along the channel the necessary asymmetry to exploit the photo-thermoelectric effect (PTE).[47] At 3 THz, the PD has NEP = 300 pWHz$^{-1/2}$ (see Supporting Information) when the bow-tie antenna axis is parallel to the polarization of the incident beam. These PTE-based GFETs PDs have broadband (from telecom[48] to THz[37] frequencies) and high-speed response times, with detection speed up to 67 GHz in the telecom band,[48] not expected to roll-off at different excitation frequencies because hot-carrier cooling timescales are set to a few picoseconds by the broadband electron-optical phonon interaction.[49] For our PDs, the measured response time is 4 ns (setup-limited), corresponding to a BW>40 MHz (see Supporting Information). The THz-induced PTE current[50] is measured under zero bias, i.e., by connecting s to the ground and the drain (d) electrode to a variable gain TIA (Femto, DHPCA-100) with adjustable BW from 220 kHz to 200 MHz. To maximize responsivity, a fixed gate voltage (V_G = -3 V) is applied via two 1.5 V batteries.

The TIA output is AC-coupled and processed through an active filtering system based on SDR architecture (Ettus Research, USRP-N210).[51] This pre-processing of the signal helps suppress spurious electronic noise components in addition to limiting intersymbol interference (ISI). An optimized Automatic Gain Control (AGC) algorithm, with a 1 ms update rate and maximum gain = 1000, dynamically keeps the SDR signal amplitude output in the 0–1 V range. A computationally efficient controllable DC-block stage with a delay line of suitable length is optimized on the specific bit rate employed.[51] A further software block performs a low-pass matched filtering with 4 MHz BW. The filtered signal is then digitized by a variable-threshold Schmitt-trigger comparator system,[44] and a second Arduino DUE board decodes and analyzes the received signal in real time.

3. Experimental Procedures and Results

In order to optimize the parameters for communication, a preliminary characterization of the setup in terms of BW and electronic noise is carried out (Section 3.1). Sequentially, we characterize the performances both in terms of received SNR and PER at RX for different signal amplitudes, controlling the optical power impinging the GFET (Section 3.2). This allows us to emulate a variable distance between TX and RX stages. The received amplitude is correlated to the distance between the source and PD, placed in the line of sight (LoS), through an atmospheric absorption and geometrical losses simulation model presented in Section 4.

3.1. Bandwidth, Noise Spectra, and Bit Rate Configurations

We first characterize the setup in terms of attainable BW. Despite both PD and QCL BWs being quite large (>50 MHz[32] and ≈1 GHz,[52] respectively), the system BW is limited, on the RX side, by the large (10^6–10^7 V A^{-1}) TIA gain needed (setting a maximum BW≈3.5 MHz) and on the TX side, by the maximum modulation BW of the current driver, ≈1.4 MHz, limiting the overall BW. These limitations can be overcome, and therefore larger communication BWs can be achieved, by on-chip pre-amplification for the GFET receiver, and by employing a faster modulator for the THz QCL.[30]

Given the BW limit ≈1.4 MHz, we select two different values for the TIA gain: G1 = 10^6 V/A, corresponding to BW≈3.5 MHz, high-speed configuration, and G2 = 10^7 V A^{-1}, corresponding to BW≈220 kHz, in low-noise configuration (equivalent input noise = 47 fA). G1 is employed to exceed the QCL modulator BW, allowing for efficient OOK communication at 1 Mbps with Manchester encoding. A higher bit rate could be employed using a current modulator with higher BWs, or different QCL supply approaches (i.e., employing a bias-tee in the QCL current feed line). G2 is used to test the maximum achievable communication distance, maximizing the signal received at RX, for lower bit rates.

The overall system BW is analyzed using an arbitrary waveform generator (Siglent SDG2042X) to generate a sinusoidal signal, which drives the QCL current supply in a small-signal regime. The frequency of this signal is varied and the peak-to-peak amplitude after TIA is recorded with an oscilloscope. The BW measurements for both TIA gain settings are in **Figure 3a**. Amplitude values are normalized to the maximum peak value and are expressed in dB. The maximum achieved bit rates are 1 Mbps OOK with Manchester encoding for G1 and 115 kbps OOK with Manchester encoding for G2, respectively.

Figure 3b shows the PD noise spectral density measured with a real-time signal analyzer (Tektronix RSA5106A, resolution BW = 1 Hz) after the TIA. The green and lilac lines represent data with laser ON driven by a continuous current of 570 mA (max laser power) and TIA in G1 and G2 configurations, respectively. The low-frequency $1/f$ noise, mainly caused by SLG mobility fluctuations,[53] is the dominant contribution of up to 10 kHz, in agreement with that reported for other devices with similar geometries.[54,55] When the GFET is illuminated by the THz beam (green and lilac traces), the light-induced excess current in the PD increases the $1/f$ noise component by a factor 2 (≈3 dB), as expected by the empirical Hooge's law,[56] which predicts that the current spectral density N_I is proportional to the square of the current flowing in the channel.[56] Between 10 kHz and 1 MHz, the noise flattens close to the expected[56] thermal noise (6 μV Hz^{-1}; the voltage spectral density N_V after the TIA is related to N_I as $N_V = gN_I$). The gain peaking ≈2 MHz is ascribed to the non-flat TIA gain.

3.2. Communication Performances of the TWC System

In order to test the communication performances of the TWC link, PER values are recorded as a function of the signal amplitude (peak-to-peak) S_{pp} at RX. S_{pp} is controllably varied by progressively attenuating the optical power impinging on the PD, and recorded by means of a 2.5 Gs/s 4-channel digital oscilloscope (Tektronix, MDO3024 200 MHz BW), connected to the TIA output. Upper panel in **Figure 4a** shows the measured PER as a function of S_{pp} for 1 Mbps (TIA gain setting G1) and 115 kbps

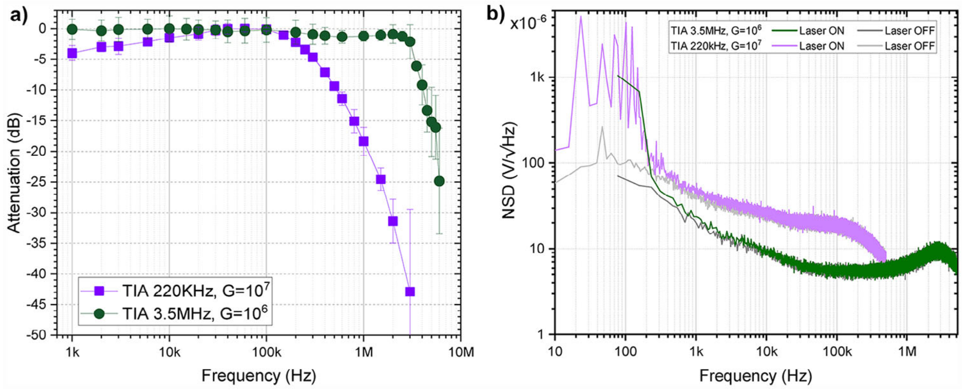

Figure 3. a) BW measurements for TIA configurations G1 (10^6 V A^{-1} gain, 3.5 MHz BW) and G2 (10^7 V A^{-1} gain, 220 kHz BW). Error bars are related to the standard deviation of the signal amplitude over 64 acquisitions. b) Noise spectral density measured with a real-time signal analyzer, in laser on and laser off conditions, for both TIA gain settings.

(TIA gain setting G2), for a fixed TX-RX distance of 0.6 m. Horizontal error bars correspond to the uncertainty of the detected signal amplitude through the oscilloscope, whereas the vertical error bars are related to the observed variance of the number of good packets received in three repeated experimental runs for a given signal amplitude. The shaded gray areas represent the error-free threshold related to the total number of sent packets. At 1 Mbps, the 125 mV threshold corresponds to a 0.65 mW impinging on the GFET PD, as shown in the lower panel of Figure 4a where measured PER is expressed as a function of the optical power impinging on the PD. The error-free threshold shifts to 570 mV (0.28 mW) at 115 kbps.

In order to provide a model estimation of the experimental PER, we consider a binary OOK modulation scheme with additive white Gaussian noise (AWGN) affecting the transmission channel and a uniform distribution of erroneous bits on the received packets. Under such conditions, the bit error rate (BER) can be estimated as $BER = 0.5erfc\sqrt{(Eb/No)}$, where Eb is the energy per bit, whilst No quantifies the noise affecting the communication channel.[57] In case no consecutive errors are occurring in a single packet, PER can be related to BER via $PER = 1 - (1 - BER)^N$,[58] where N = 32 is the number of bits constituting the transmitted packets. Combining these relations, we get[57]:

$$PER = 1 - \left\{ 1 - 0.5erfc\left[\frac{S}{\left(2w\sqrt{2}\right)} \right] \right\}^N \tag{1}$$

Red and blue thick solid lines of Figure 4a (upper panel) represent the fit with w as a free parameter, yielding $w_{G1} = 12.8$ mV and $w_{G2} = 57$ mV for 1 Mbps and 115 kbps, respectively. The larger noise value for 115 kbps as compared to 1 Mbps stems from the larger gain settings. Despite the AWGN assumption not being fully valid in the overall detector BW for both gain settings (2–3.5 kHz and 5–220 kHz, respectively), as shown by the NSD spectra of Figure 3b, $w_{G2}/w_{G1} \approx 4.5$ is still compatible with the average NSD ratio in the central portion of the spectrum (1–100 kHz). Moreover, upon analyzing the RMS noise values measured with an oscilloscope for the two different configurations, we note that the recorded values stand at 9.6 mV and 61 mV for 1 Mbps and 115 kbps, respectively. These measured values align closely with the values derived from the fitting process, denoted as w_{G1} and w_{G2}. In Figure 4a (lower panel) we replot PER data as a function of optical power. This clearly shows that a larger communication bandwidth globally requires more power from the laser source reaching the detector, to recover an acceptable energy-per-bit value (Eb). Conversely, the trend may seem reversed when ex-

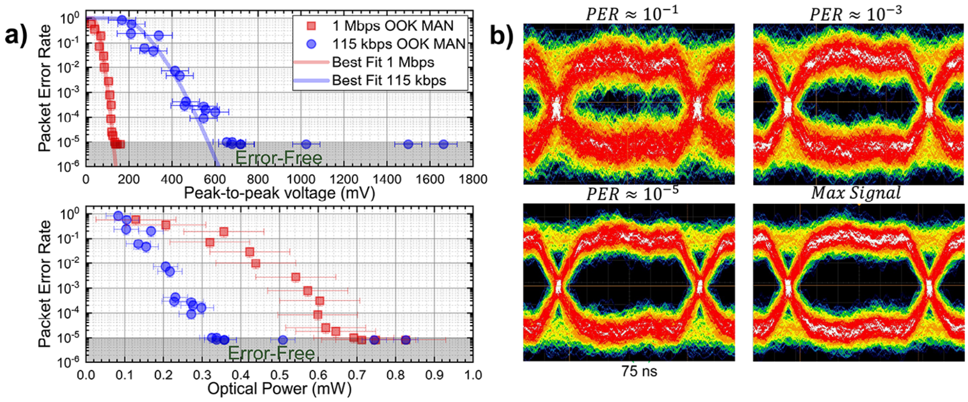

Figure 4. a) Upper panel: PER versus peak-to-peak amplitude for 1 Mbps and 115 kbps OOK Manchester (MAN) with fitting model. Lower panel: PER versus optical power for 1 Mbps and 115 kbps OOK Manchester (MAN). b) Eye Diagrams at 1 Mbps for different PERs.

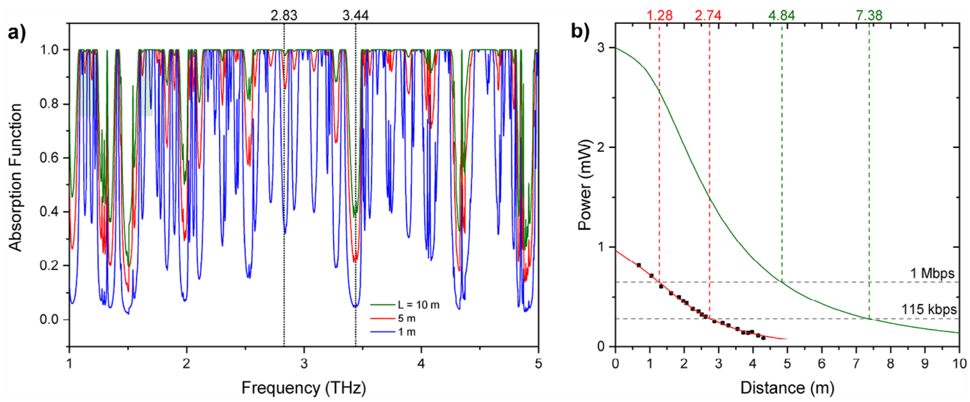

Figure 5. a) Absorption function (i.e., $[1 - exp(-kL)]$, where k is the absorption coefficient of the gas mixture and L is the optical path length) of the atmospheric gas mixture for 3 optical path lengths taken from Hitran database,[60] relative to high latitude, summer conditions. The two vertical dashed lines represent the two considered QCL frequencies: 2.83 THz is the central frequency of the QCL employed in our setup, and 3.44 THz is the lasing frequency of a QCL matching a higher transparency window. b) Power as a function of distance (black squares), taking into consideration long-distance propagation losses due to atmospheric absorption and geometrical losses. A fit taking into account the details of our setup is shown, for a fixed k1 = 0.0025 cm^{-1} absorption coefficient, measured in lab conditions. The resulting fit parameters are W_0= 0.385 cm, z_R= 95 cm, P_0= 0.967 mW (red line). By using this model, it is possible to simulate the performances of our THz FSOL employing a different QCL source, i.e., a 3 mW device operating at 3.44 THz.

pressing PER as a function of the measured peak-to-peak voltage after the TIA stage (Figure 4a upper panel) owing to the different gain settings employed in the two communication bandwidths, where a larger gain corresponds to lower bandwidth. Figure 4b presents eye diagrams at 1 Mbps for various signal amplitudes (160, 145, 100, 70 mV) corresponding to different PERs from PER = 10^{-1} down to the error-free threshold (PER = 10^{-5}). Eye patterns, reported with normalized width in Figure 4b to better highlight the progressive impact of noise, are generated by replacing the transmitter with a BERT module (FarSite, FarSync Flex) outputting a (2^9–1) bit-long pseudorandom binary sequence (PRBS) and recording the RX output signal using a digital oscilloscope (Keysight, DSOX6004A) after the TIA stage before data processing.

4. Estimation of OWC THz Link Lengths in Free-Space Propagation

4.1. Relation Between Signal Amplitude and TX-RX Distance

In order to emulate the losses on the THz channel due to free-space propagation in longer distances as compared to those available in the laboratory, we estimate the performance in realistic conditions, by combining the PER results with the predictions of a propagation model estimating the atmospheric and geometrical losses for our THz beam. We neglect scattering phenomena, as the THz radiation is particularly robust to these, and all measurements are taken in laboratory conditions. We assume two main sources of losses, progressively reducing the fraction of power collected by the detector:

1) absorption of the THz radiation by water vapor;
2) geometrical losses on the THz beam.

Regarding 1), **Figure** 5a reports the water vapor absorption in the whole spectral range where THz QCLs operate, ≈1.2–4.9 THz,[59] for three different link lengths: 1, 5, 10 m. Figure 5a highlights that water absorption is considerable in the whole range, but favorable transparency windows exist at specific wavelengths. Despite our device, operating at 2.83 THz, not being optimized for THz FSOC, considering the wavelength flexibility of QCL technology,[59] the performance of our THz FSOC link can be boosted by embedding a QCL operating in a more favorable transmission window, i.e., ≈3.44 THz, where QCLs have optimal performances. In our laboratory conditions, i.e., 35% relative humidity at 23 °C, the absorption coefficient retrieved from the Hitran database[60] at 2.83 THz is $k_1 = 0.0025$ cm^{-1}. In the same conditions, a 3.44 THz QCL would feature a fourfold reduction in the absorption coefficient ($k_2 = 0.00058$ cm^{-1}).

In order to estimate the geometrical losses on the propagation of the THz beam, we consider a model based on measurements of THz optical power at different distances from the QCL source. We assume a Gaussian intensity distribution for the THz beam, with an effective waist radius W_0 in the position z_f along the beam path. By defining the Rayleigh parameter z_R and the total optical power P_0, the intensity distribution at a distance z from the exit pupil of the collimating mirror can be expressed as[61]:

$$I\ (r, z) = \frac{2P_0}{\pi W_0^2}\ exp\left[\frac{-2r^2}{W_0^2\left(1 + \left(z - z_f\right)^2 / z_R^2\right)}\right] \tag{2}$$

Assuming the beam axis is perfectly aligned with the center of the aperture of the receiver mirror of radius R_d, the overall power collected by the receiver at a distance z can be calculated by integrating the intensity over the aperture of the collection mirror:

$$P\ (z) = P_0\ exp\,(-kz)\left\{1 - exp\left[\frac{-R_d^2}{W_0^2\left(1 + \left(z - z_f\right)^2 / z_R^2\right)}\right]\right\} \tag{3}$$

where k is the absorption coefficient of water vapor.

By measuring the optical power impinging on the RX stage at different distances from the QCL source in the range from 0.5 to 4.5 m (black dots in Figure 5b), we use Equation (3) to fit the data and retrieve the propagation model for our THz beam (solid red line in Figure 5b). Data are taken by using a THz power meter (Ophir 3A-P-THz) and a parabolic mirror with the same aperture as the one used for the GFET detector (1″). In the fit, we use an absorption coefficient $k_1 = 0.0025$ cm^{-1}, corresponding to our laboratory conditions. The horizontal dashed lines in Figure 5b represent the minimum power required for error-free communication for 1 Mbps and 115 kbps (0.65 mW and 0.28 mW, respectively). These correspond to THz link lengths of 128 and 274 cm, respectively, representing the largest error-free distances attainable. These are of the same order of magnitude of those achieved in previous THz QCL-based setups needing deep cryogenic temperatures both for laser sources (≈10 K) and PDs (≈4 K).[18–20] By inserting a different absorption coefficient in our propagation model, it is possible to reconstruct the power versus distance curves for a source emitting at a different wavelength, matching a more favorable atmospheric transparency window. Selecting a QCL emitting at 3.44 THz, in the same humidity lab conditions ($k_2 = 0.00058$ cm^{-1}), and with a 3 mW optical power, an underestimation of what is already commercially available,[62] we obtain the green solid line in Figure 5b. Our predictions show enhanced link lengths of ≈5 and 7.5 m at 1 Mbps and 115 kbps, respectively. This would not require any other change in our transportable THz FSOC setup, except replacing the QCL chip with a 3.44 THz one. A different geometrical configuration can be devised to minimize the geometric losses. Replacing the 1″ parabolic mirrors with a wider diameter (e.g., 3″), would drastically reduce the divergence of the beam. Adaptive optics could be employed in order to maximize the signal received at RX.

5. Conclusion

We demonstrated a THz wireless communication link employing a transportable and cryogen-free setup. This uses a directly modulated QCL source at 2.83 THz, hosted in a closed-cycle Stirling cryocooler, and an RT GFET PD. We report error-free communication (PER<10^{-5}) over 60 cm at 1 Mbps OOK with Manchester encoding, limited by the gain/BW parameter of the TIA amplification stage. By performing power over distance measurements, we quantified the losses over the THz link, combining both molecular absorption phenomena and geometric losses. This resulted in a 128 cm error-free distance at 1 Mbps, and 274 cm at 115 kbps, demonstrating that our cryogen-free setup exhibits state-of-the-art performances, competitive with respect to those of bulky and more expensive liquid-He-cooled TWCs. We presented a propagation model allowing us to predict the communication performance in atmospheric propagation, when employing an optimized 3 mW, 3.44 THz QCL source, matching a more favorable atmospheric transparency window. The estimated error-free distance at 1 Mbps reaches ≈5 m, and ≈7.5 m at 115 kbps, which can be further enhanced with optimized geometrical configurations. Our QCL and GFET technologies present much higher BW capabilities that can be unlocked by technical improvements on the TX and RX stages.

Our cryogen-free, transportable TWC system lays the foundations for the deployment of QCL-based THz wireless communications, with reduced complexity and costs, requiring no expensive and bulky cooling systems. This is promising for both terrestrial and satellite THz communication, where reliability, ease of operation, and reduced payload are essential.

Supporting Information

Supporting Information is available from the Wiley Online Library or from the author.

Acknowledgements

Authors acknowledge funding from Consiglio Nazionale delle Ricerche (Progetti di Ricerca @CNR, "TEROCODE" and "FluoCom" projects), Laboratori congiunti ASI-CNR nel settore delle Quantum Technologies (Q-ASINO) funded by ASI and CNR (Accordo Attuativo n.2023-47-HH.0) the European Union Graphene Flagship (core 3), by the ERC Grants (681379) SPRINT, and by the European Union under the Italian National Recovery and Resilience Plan (NRRP) of Next Generation EU, partnership on "Telecommunications of the Future" (PE00000001 - program "RESTART", Structural Project DREAMS, EPSRC Grants EP/K01711X/1, EP/K017144/1, EP/N010345/1, EP/L016087/1, EP/X015742/1, EP/V000055/1, ERC grants Hetero2D, GSYNCOR, GIPT, EU grant Graph-X, European Union - NextGeneration EU, "Integrated infrastructure initiative in Photonic and Quantum Sciences" - I-PHOQS [IR0000016, ID D2B8D520, CUP B53C22001750006], European Union's QuantERA II [G.A. n. 101017733] - QATACOMB Project "Quantum correlations in terahertz QCL combs" (Funding organisations: CNR - Italy).

Open access publishing facilitated by Consiglio Nazionale delle Ricerche, as part of the Wiley - CRUI-CARE agreement.

Conflict of Interest

The authors declare no conflict of interest.

Data Availability Statement

The data that support the findings of this study are available from the corresponding author upon reasonable request.

Keywords

cryogen-free, free-space optical links, FSO communications, GFET, optical wireless communications, quantum cascade lasers (QCL)

Received: October 25, 2023
Revised: October 14, 2024
Published online: December 23, 2024

[1] Cisco Systems, Zettabyte era trends and analysis, http://www.cisco.com/c/en/us/solutions/collateral/service-provider/visual-networking-index-vni/VNI_Hyperconnectivity_WP.pdf, (accessed: November **2024**).
[2] Ericsson.com, Mobile data traffic outlook, https://www.ericsson.com/en/reports-and-papers/mobility-report/dataforecasts/mobile-traffic-forecast, (accessed: November **2024**).
[3] G. Papagiannakis, G. Singh, N. Magnenat-Thalmann, *Comput. Animat. Virtual Worlds* **2008**, *19*, 3.

[4] C. S. Pattichis, E. Kyriacou, S. Voskarides, M. S. Pattichis, R. Istepanian, C. N. Schizas, *IEEE Antennas Propag. Mag.* **2002**, *44*, 143.
[5] Y. T. Shen, L. Chen, W. W. Yue, H. X. Xu, *Front. Med.* **2021**, *8*, 646506.
[6] M. Mahmood, D. Mzurikwao, Y. S. Kim, Y. Lee, S. Mishra, R. Herbert, A. Duarte, C. S. Ang, W. H. Yeo, *Nat. Mach. Intell.* **2019**, *1*, 412.
[7] J. D. Simeral, T. Hosman, J. Saab, S. N. Flesher, M. Vilela, B. Franco, J. N. Kelemen, D. M. Brandman, J. G. Ciancibello, P. G. Rezaii, E. N. Eskandar, *IEEE Trans. Biomed. Eng.* **2021**, *68*, 2313.
[8] M. Giordani, M. Polese, M. Mezzavilla, S. Rangan, M. Zorzi, *IEEE Commun. Magazine* **2020**, *58*, 55.
[9] M. Saad, F. Bader, J. Palicot, Y. Corre, G. Gougeon, J.-B. Doré, BRAVE D1.0, Supelec; CEA, Available online, https://hal.archives-ouvertes.fr/hal-01947363/document, **2018**.
[10] C. Bowdery, S. Patel, Bringing 5G networks indoors, https://www.ericsson.com/en/blog/6/2024/imagine-studio-unboxed-bringing-5g-indoors-enhancing-connectivity, (accessed: November **2024**).
[11] M. Alsabah, M. A. Naser, B. M. Mahmmod, S. H. Abdulhussain, M. R. Eissa, A. Al-Baidhani, N. K. Noordin, S. M. Sait, K. A. Al-Utaibi, F. Hashim, *IEEE Access* **2021**, *9*, 148191.
[12] D. Serghiou, M. Khalily, T. W. C. Brown, R. Tafazolli, *IEEE Commun. Surveys & Tutorials* **2022**, *24*, 1957.
[13] P. Porambage, G. Gür, D. P. Moya Osorio, M. Livanage, M. Ylianttila, in Proc. 2021 Joint European Conference on Networks and Communications & 6G Summit (EuCNC/6G Summit), Porto, Portugal, **2021**, pp. 622–627.
[14] W. Jiang, B. Han, M. A. Habibi, H. D. Schotten, *IEEE Open J. Commun. Soc.* **2021**, *2*, 334.
[15] C. D. Alwis, A. Kalla, Q. V. Pham, P. Kumar, K. Dev, W. J. Hwang, M. Liyanage, *IEEE Open J. Commun. Soc.* **2021**, *2*, 836.
[16] H. Tataria, M. Shafi, M. Dohler, S. Sun, *IEEE Vehicular Technology Magazine* **2022**, *17*, 16.
[17] J. Rodriguez in, *Fundamentals of 5G Mobile Networks*, John Wiley & Sons, Hoboken NJ **2014**, Ch7.
[18] X. You, X. C. Wang, J. Huang, X. Gao, Z. Zhang, M. Wang, Y. Huang, C. Zhang, Y. Jiang, J. Wang, M. Zhu, *Sci. China Inf. Sci.* **2021**, *64*, 110301.
[19] T. Nagatsuma, S. Horiguchi, Y. Minamikata, Y. Yoshimizu, S. Hisatake, S. Kuwano, N. Yoshimoto, J. Terada, H. Takahashi, *Opt. Express* **2013**, *21*, 23736.
[20] D. M. Slocum, E. J. Slingerland, R. H. Giles, T. M. Goyette, *J. Quant. Spectrosc. Radiat. Transfer* **2013**, *127*, 49.
[21] Z. Fang, H. Guerboukha, R. Shrestha, M. Hornbuckle, Y. Amarasinghe, D. M. Mittleman, *IEEE Trans. Terahertz Sci. Technol.* **2022**, *12*, 363.
[22] M. Civas, O. B. Akan, *ITU J. Future Evolving Technol.* **2021**, *2*, 7.
[23] S. Koenig, D. Lopez-Diaz, J. Antes, F. Boes, R. Henneberger, A. Leuther, A. Tessmann, R. Schmogrow, D. Hillerkuss, R. Palmer, T. Zwick, C. Koos, W. Freude, O. Ambacher, J. Leuthold, I. Kallfass, *Nat. Photonics* **2013**, *7*, 977.
[24] K. Ishigaki, M. Shiraishi, S. Suzuki, M. Asada, N. Nishiyama, S. Arai, *Electron. Lett.* **2012**, *48*, 582.
[25] T. Nagatsuma, G. Ducournau, C. C. Renaud, *Nat. Photonics* **2016**, *10*, 371.
[26] X. Pang, S. Jia, O. Ozolins, X. Yu, H. Hu, L. Marcon, P. Guan, F. Da Ros, S. Popov, G. Jacobsen, M. Galili, T. Morioka, D. Zibar, L. K. Oxenløwe, in Proc. IEEE Photonics Conf., IEEE, Waikoloa, HI, USA, **2016**.
[27] S. Jia, X. Pang, O. Ozolins, X. Yu, H. Hu, J. Yu, P. Guan, F. Da Ros, S. Popov, G. Jacobsen, M. Galili, T. Morioka, D. Zibar, L. K. Oxenløwe, *J. Lightwave Technol.* **2018**, *36*, 610.
[28] R. Köhler, A. Tredicucci, F. Beltram, H. E. Beere, E. H. Linfield, A. G. Davies, D. A. Ritchie, R. C. Iotti, F. Rossi, *Nature* **2022**, *417*, 156.
[29] H. Schneider, H. C., *Liu Quantum Well Infrared Photodetectors-Physics and Applications*, Springer-Verlag, Berlin Heidelberg **2007**.
[30] L. Gu, Z. Tan, Q. Wu, C. Wang, J. Cao, *Chin. Opt. Lett.* **2015**, *13*, 081402.
[31] Z. Chen, L. Gu, Z. Tan, C. Wang, J. Cao, *Chin. Opt. Lett.* **2013**, *11*, 112001.
[32] Z. Tan, Z. Chen, J. Cao, H. Liu, *Chin. Opt. Lett.* **2013**, *11*, 031403.
[33] A. Khalatpour, A. K. Paulsen, C. Deimert, Z. R. Wasilewski, Q. Hu, *Nat. Photonics* **2021**, *15*, 16.
[34] B. T. Bulcha, J. L. Hesler, V. Drakinskiy, J. Stake, A. Valavanis, P. Dean, L. H. Li, N. S. Barker, *IEEE Trans. Terahertz Sci. Technol.* **2016**, *6*, 737.
[35] N. Daghestani, K. Parow-Souchon, D. Pardo, H. Liu, N. Brewster, M. Frogley, G. Cinque, B. Alderman, P. G. Huggard, *Infrared Phys. Technol.* **2019**, *99*, 240.
[36] E. Javadi, D. B. But, K. Ikamas, J. Zdanevičius, W. Knap, A. Lisauskas, *Sensors* **2021**, *21*, 2909.
[37] L. Viti, A. Cadore, X. Yang, A. Vorobiev, J. Muench, K. Watanabe, T. Taniguchi, J. Stake, A. C. Ferrari, M. S. Vitiello, *Nanophotonics* **2020**, *10*, 89.
[38] M. Asgari, E. Riccardi, O. Balci, D. De Fazio, S. M. Shinde, J. Zhang, S. Mignuzzi, F. H. L. Koppens, A. C. Ferrari, L. Viti, M. S. Vitiello, *ACS Nano* **2021**, *15*, 17966.
[39] B. Hinkov, A. Hugi, M. Beck, J. Faist, *Opt. Express* **2016**, *24*, 3294.
[40] F. Capasso, R. Paiella, R. Martini, R. Colombelli, C. Gmachl, T. L. Myers, M. S. Taubman, R. M. Williams, C. G. Bethea, K. Unterrainer, H. Y. Hwang, *IEEE J. Quantum Electron.* **2002**, *38*, 511.
[41] *IEEE Standard for Local and metropolitan area networks–Part 15*, Vol. *7*, IEEE Std 802.15.7-2018, Piscataway, NJ, USA (Revision of IEEE Std 802.15.7-2011), IEEE Standards, New York City **2019**.
[42] Arduino, Arduino DUE webpage, https://docs.arduino.cc/hardware/due, (accessed: November, **2024**).
[43] M. Seminara, T. Gabbrielli, N. Corrias, S. Borri, L. Consolino, M. Meucci, P. De Natale, F. Cappelli, J. Catani, *Opt. Express* **2022**, *30*, 44640.
[44] T. Nawaz, M. Seminara, S. Caputo, L. Mucchi, F. S. Cataliotti, J. Catani, *IEEE Transac. Vehic. Technol.* **2019**, *68*, 12040.
[45] M. S. Vitiello, G. Scamarcio, V. Spagnolo, S. S. Dhillon, C. Sirtori, *Appl. Phys. Lett.* **2007**, *90*, 19.
[46] L. Viti, D. G. Purdie, A. Lombardo, A. C. Ferrari, M. S. Vitiello, *Nano Lett.* **2020**, *20*, 3169.
[47] D. A. Bandurin, I. Gayduchenko, I. Cao, M. Moskotin, A. Principi, I. V. Grigorieva, G. Goltsman, G. Fedorov, D. Svintsov, *Appl. Phys. Lett.* **2018**, *112*, 141101.
[48] V. Mišeikis, S. Marconi, M. A. Giambra, A. Montanaro, L. Martini, F. Fabbri, S. Pezzini, G. Piccinini, S. Forti, B. Terrés, I. Goykhman, L. Hamidouche, P. Legagneux, V. Sorianello, A. C. Ferrari, F. H. L. Koppens, M. Romagnoli, C. Coletti, *ACS Nano* **2020**, *14*, 11190.
[49] E. A. A. Pogna, X. Jia, A. Principi, A. Block, L. Banszerus, J. Zhang, X. Liu, T. Sohier, S. Forti, K. Soundarapandian, B. Terrés, J. D. Mehew, C. Trovatello, C. Coletti, F. H. L. Koppens, M. Bonn, H. I. Wang, N. van Hulst, M. J. Verstraete, H. Peng, Z. Liu, C. Stampfer, G. Cerullo, K. H. Tielrooij, *ACS Nano* **2021**, *15*, 11285.
[50] M. Massicotte, G. Soavi, A. Principi, K. J. Tielrooij, *Nanoscale* **2021**, *13*, 8376.
[51] M. A. Umair, M. Meucci, J. Catani, *Sensors* **2023**, *23*, 1594.
[52] D. Oustinov, N. Jukam, R. Rungsawang, J. Madéo, S. Barbieri, P. Filloux, C. Sirtori, X. Marcadet, J. Tignon, S. Dhillon, *Nat. Commun.* **2010**, *1*, 69.
[53] A. Rehman, J. A. Delgado Notario, J. S. Sanchez, Y. M. Meziani, G. Cywiński, W. Knap, A. A. Balandin, M. Levinshtein, S. Rumyantsev, *Nanoscale* **2022**, *14*, 7242.
[54] M. Asgari, L. Viti, O. Balci, S. M. Shinde, J. Zhang, H. Ramezani, S. Sharma, A. Meersha, G. Menichetti, C. McAleese, B. Conran, X. Wang, A. Tomadin, A. C. Ferrari, M. S. Vitiello, *Appl. Phys. Lett.* **2022**, *121*, 031103.

[55] G. Liu, W. Stillman, S. Rumyantsev, Q. Shao, M. Shur, A. A. Balandin, *Appl. Phys. Lett.* **2009**, *95*, 033103.
[56] A. A. Balandin, *Nat. Nanotechnol.* **2013**, *8*, 549.
[57] H. Stern, S. Mahmoud, L. Stern, *Communication Systems: Analysis and Design*, Pearson Prentice Hall, London **2004**.
[58] R. Khalili, K. Salamatian, Presented at *3rd Annual Communication Networks and Services Research Conference (CNSR'05)*, IEEE, **2005**.
[59] M. S. Vitiello, G. Scalari, B. Williams, P. De Natale, *Opt. Express* **2015**, *23*, 5167.
[60] Gas Mixtures, HITRAN on the web, https://hitran.iao.ru/gasmixture, (accessed: November **2024**).
[61] A. E. Siegman, in Proc. SPIE 1868, Laser Resonators and Coherent Optics: Modeling, Technology, and Applications, **1993**.
[62] T. C Lytid., 2000 series, https://lytid.com/products/terahertz/teracascade2000/(accessed: November, **2024**).

